

Article

Analysis of Subsynchronous Torsional of Wind–Thermal Bundled System Transmitted via HVDC Based on Signal Injection Method

Junxi Wang, Qi Jia *, Gangui Yan, Kan Liu and Dan Wang

Ministry of Education Key Laboratory of Modern Power System Simulation Control and Green Power Technology, Northeast Electric Power University, Jilin 132012, China; 2201900091@neepu.edu.cn (J.W.); yangg@neepu.edu.cn (G.Y.); 2201900191@neepu.edu.cn (K.L.); 1201600005@neepu.edu.cn (D.W.)

* Correspondence: 2201800207@neepu.edu.cn; Tel.: +86-159-4869-2960

Abstract: With the development of large-scale new energy, the wind–thermal bundled system transmitted via high-voltage direct current (HVDC) has become the main method to solve the problem of wind power consumption. At the same time, the problem of subsynchronous oscillation among wind power generators, high-voltage direct current (HVDC), and synchronous generators (SGs) has become increasingly prominent. According to the dynamic interaction among doubly fed induction generators (DFIGs), HVDC, and SGs, a linearization model of DFIGs and SGs transmitted via HVDC is established, and the influence of the electromagnetic transient of wind turbines and HVDC on the electromechanical transient processes of SGs is studied. Using the method of additional excitation signal injection, the influence of the main factors of DFIG on the damping characteristics of each torsional mode of SG is analyzed, including control parameters and operation conditions when the capacity of HVDC is fixed. The mechanism of the negative damping torsional of SGs is identified. A time-domain simulation model is built in Electromagnetic Transients including DC/Power Systems Computer Aided Design (EMTDC/PSCAD) to verify the correctness and effectiveness of the theoretical analysis.

Keywords: doubly fed induction generator; synchronous generator; high-voltage direct current; electromechanical coupling; shaft torsion



Citation: Wang, J.; Jia, Q.; Yan, G.; Liu, K.; Wang, D. Analysis of Subsynchronous Torsional of Wind–Thermal Bundled System Transmitted via HVDC Based on Signal Injection Method. *Energies* **2021**, *14*, 474. <https://doi.org/10.3390/en14020474>

Received: 22 December 2020

Accepted: 12 January 2021

Published: 17 January 2021

Publisher's Note: MDPI stays neutral with regard to jurisdictional claims in published maps and institutional affiliations.



Copyright: © 2021 by the authors. Licensee MDPI, Basel, Switzerland. This article is an open access article distributed under the terms and conditions of the Creative Commons Attribution (CC BY) license (<https://creativecommons.org/licenses/by/4.0/>).

1. Introduction

In recent years, developing wind resources vigorously has been an important way of promoting energy transition and meeting the environmental challenges [1,2]. In the first half of 2020, China's new grid-connected installed capacity was 6.32 million MW. By the end of June, the installed capacity of wind power was 217 million kW [3], and the installed wind power capacity has increased steadily. It is estimated that, by 2050, the installed wind power capacity will reach 2.4 billion kW in China [4].

Due to the uncoordinated distribution of wind power resources and load development in China, there is a problem of wind power accommodation. Wind power requires large-scale, long-distance, and stable transportation. Thus, the wind–thermal bundled system transmitted via high-voltage direct current (HVDC) is the key means to solve this problem, such as the Lugu HVDC project and Hazheng HVDC project. However, while solving the problem of accommodation, the security and stability of the sending network face hidden risks [5,6], example.g., the problem of power oscillation. In July 2015, a subsynchronous oscillation (SSO) occurred in a wind farm in Hami, Xinjiang, China, which caused the shaft torsional oscillation of the synchronous generator (SG) at a distance of 300 km, threatening the safe operation of the system [7,8].

Focusing on the power oscillation problem of the sending network, domestic and foreign scholars have investigated the following aspects using the eigenvalue method,

complex torque coefficient approach, impedance analysis approach, etc: (1) the problem of SSO in SGs via HVDC transmission [9–11]; (2) the SSO of wind turbines transmitted via HVDC [12–15]; (3) the SSO of wind–thermal bundled systems transmitted via HVDC [16–18].

In the research of SGs via HVDC transmission, [9] pointed out that the HVDC transmission capacity, strength of grid, and current loop control strategy all affect the torsional vibration of the SG shafting and induce 11.5 Hz negative damping oscillation. The authors of [10,11] studied the stability mechanism of SSO caused by HVDC using the complex torque coefficient method, as well as pointed out that the nearby generators can produce SSO negative damping when the bandwidth of the constant current controller on the rectifier side is 10–20 Hz. In terms of wind turbines via HVDC transmission, [12,13] used the eigenvalue method and complex torque coefficient approach to study doubly fed induction generator (DFIG) and HVDC system wind farm damping characteristics, showing that their interaction is not obvious. The influence of DFIG controller parameters and wind speed on the torsional mode of SG was evaluated using eigenvalue analysis in [14]. The results showed that the frequency and damping of the torsional mode increased when the rotor-side converter power outer loop parameter increased from 1 to 5 or the current inner loop control parameter changed from 0.1 to 10; on the other hand, when the wind speed increased from 11 m/s to 15 m/s, the torsional mode first decreased and then increased. The authors of [15] pointed out that the damping of the SSO increases, and the coupling mechanism was deduced as a function of the dynamic process between voltage and current disturbance at the coupling point, when the proportional coefficient of the permanent magnetic synchronous generator (PMSG) outer loop and HVDC constant current controller increased or the integral coefficient decreased.

The research on the interaction between SGs or wind turbines and HVDC has been relatively complete, but the research on the interaction of wind turbines, SGs, and HVDC is still rare. The oscillation mechanism of the wind–thermal bundled system transmitted via HVDC was evaluated using a time-domain simulation and eigenvalue analysis in [16,17], pointing out that the connection of DFIG can alleviate the SSO of SGs caused by HVDC. The authors of [18] proposed an active disturbance rejection additional damping control using the least square to suppress the shaft torsional vibration of the wind–thermal bundled system effectively transmitted via HVDC. However, the dynamic interaction mechanism among the three has not been fully explained.

In wind–thermal bundled systems transmitted via HVDC, the torsional vibration of the SG caused by grid-connected wind turbines is manifested in the rotor speed oscillation. To be specific, the speed contains abundant electromechanical coupling information. If a certain controllable disturbance is applied to stimulate speed oscillation, we can observe the characteristics of speed response after the disturbance is removed, as well as judge the electromechanical coupling characteristics among wind turbines, HVDC, and SGs, and the contribution of various factors to torsional vibration can be identified.

Unlike previous studies, this paper proposes using the signal injection method to analyze the torsional vibration of a high-proportion wind power system [19], which involves applying an alternating current (AC) voltage signal on the excitation winding to stimulate speed oscillation. This paper observes the difference of the free response characteristics of the speed disturbance, which is caused by the change in wind turbine scale, and it identifies the coupling mechanism of DFIGs, HVDC, and SG shafting. The main contributions of this paper are as follows:

- The linearization models of DFIGs and SGs transmitted via HVDC are established. Thus, the influence of the electromagnetic transient process of wind turbines and HVDC on the electromechanical transient process of SGs is studied. Moreover, this paper reveals the interaction mechanism of the system;
- The influences of DFIG control parameters and operating conditions on the damping characteristics of each torsional mode of SGs under the condition of a fixed capacity of

- HVDC is analyzed on the basis of injection signal identification. Then, the negative damping torsional vibration mechanism of the SG shafting system is identified;
- Considering the differences in operation conditions and control parameters of different DFIGs in the wind farm, taking two-machine parallel systems as an example, the influence of DFIGs on the torsional vibration of SG shafting is further expounded.

2. System Model

The topological structure of a wind–thermal bundled system transmitted via HVDC is shown in Figure 1, which mainly includes DFIGs, SGs, and HVDC. Considering that the DFIG in the actual system consists of hundreds and even thousands of wind turbines, the model order is high; therefore, it is difficult to establish a detailed model. Therefore, this paper establishes a single-machine model for DFIGs using the principle of similar transformation, while the model of the SG is taken from the first sub-synchronous resonance (SSR) benchmark [20], and the CIGRE Benchmark Model is used for HVDC [21].

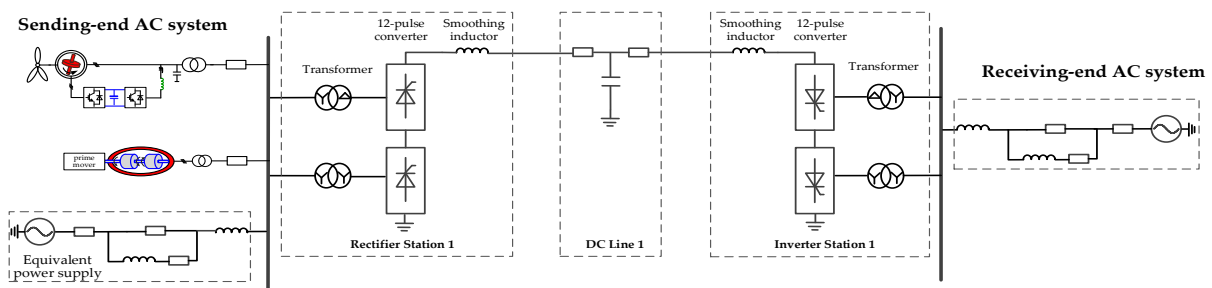


Figure 1. Structure of doubly fed induction generator (DFIG) wind farm connected with series compensated transmission network.

2.1. Model of DFIG

The DFIG topology structure and its control strategy are shown in Figure 2, consisting of wind turbines, an induction generator, a rotor-side converter (RSC), and a grid-side converter (GSC). The definitions of variables in Figure 2 are shown in Table A1 (Appendix A). The stator is directly connected to the network, and the rotor is connected to the grid through the RSC and GSC. The RSC and GSC usually use voltage vector-oriented control [22,23]. In order to maximize the utilization of wind energy, the RSC adopts the maximum power point tracking (MPPT) control strategy, whereas the GSC takes DC voltage and reactive power as the control targets.

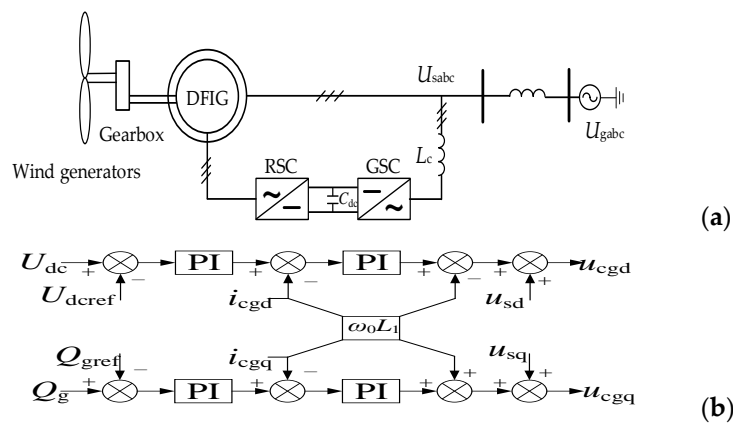


Figure 2. Cont.

where A_{HVDC} , B_{HVDC} , C_{HVDC} , and D_{HVDC} are the state matrix, input matrix and output matrix of HVDC; the state variables are $\Delta x_{HVDC} = [\Delta I_{rd}, \Delta I_{rq}, \Delta I_{dc1}, \Delta I_{dc2}, \Delta V_{dc}, \Delta V_{pccd}, \Delta V_{pccq}, \Delta V_{cr2d}, \Delta V_{cr2q}, \Delta I_{Lr1d}, \Delta I_{Lr1q}, \Delta V_{cr3d}, \Delta V_{cr3q}, \Delta V_{cr4d}, \Delta V_{cr4q}, \Delta I_{Lr2d}, \Delta I_{Lr2q}, \Delta x_9 \sim \Delta x_{12}]$, and Δx_{HVDC} is a 21×1 matrix; the input and output variables are $\Delta u_{HVDC} = [\Delta V_{rd}, \Delta V_{rq}, \Delta I_{dc}]^T$ and $\Delta y_{HVDC} = [\Delta I_{rd}, \Delta I_{rq}]^T$, and Δu_{HVDC} is a 3×1 matrix and Δy_{HVDC} is a 2×1 matrix. The definitions of variables are shown in Table A3 (Appendix A).

The transfer function of HVDC can be obtained as shown in Equation (6):

$$\Delta Y_{HVDC} = C_{HVDC} \cdot (sI - A_{HVDC})^{-1} \cdot B_{HVDC} + D_{HVDC}. \quad (6)$$

3. Electromechanical Coupling Characteristics of Equipment

According to the SG linearized model, the electromagnetic torque disturbance ΔT_e can be expressed as shown in Equation (7).

$$\Delta T_e = - \left\{ \begin{bmatrix} i_{q0} & -i_{d0} \end{bmatrix} + \begin{bmatrix} -\psi_{q0} & \psi_{d0} \end{bmatrix} \cdot \begin{bmatrix} L_1(s) & 0 \\ 0 & L_2(s) \end{bmatrix} \right\} \cdot \begin{bmatrix} s/\omega_{base} & -\omega_0 \\ \omega_0 & s/\omega_{base} \end{bmatrix}^{-1} \cdot \begin{bmatrix} -\psi_{q0} \\ \psi_{d0} \end{bmatrix} \cdot \Delta \omega_r \\ + \left\{ \begin{bmatrix} i_{q0} & -i_{d0} \end{bmatrix} + \begin{bmatrix} -\psi_{q0} & \psi_{d0} \end{bmatrix} \cdot \begin{bmatrix} L_1(s) & 0 \\ 0 & L_2(s) \end{bmatrix} \right\} \cdot \begin{bmatrix} s/\omega_{base} & -\omega_0 \\ \omega_0 & s/\omega_{base} \end{bmatrix}^{-1} \cdot \begin{bmatrix} \Delta u_d \\ \Delta u_q \end{bmatrix}, \quad (7)$$

where ω_0 is the SG rotor speed initial value, ω_{base} is the reference value of the SG, and $\omega_{base} = 60$ Hz.

$L_1(s)$ and $L_2(s)$ represent the transfer function relationship between current and flux, and the expressions are denoted in Equation (8).

$$\begin{cases} L_1(s) = \frac{(\tau_{d0}''s+1)(\tau_{d0}'s+1)}{(\tau_q''s+1)(\tau_d's+1)L_d} \\ L_2(s) = \frac{(\tau_{q0}''s+1)(\tau_{q0}'s+1)}{(\tau_q''s+1)(\tau_q's+1)L_q} \end{cases}. \quad (8)$$

According to Equation (7), the SG electromagnetic torque disturbance is related to the rotor speed disturbance and voltage disturbance, and the voltage disturbance is correlated with the current disturbance and grid structure. The expression of voltage disturbance is considered as shown in Equation (9).

$$\begin{bmatrix} \Delta u_d \\ \Delta u_q \end{bmatrix} = \begin{bmatrix} Z_{11} & Z_{12} \\ Z_{21} & Z_{22} \end{bmatrix} \cdot \begin{bmatrix} \Delta i_d \\ \Delta i_q \end{bmatrix}, \quad (9)$$

where Z_{11} , Z_{12} , Z_{21} , and Z_{22} are the grid impedance matrix elements, and the current disturbance expression is shown in Equation (10).

$$\begin{bmatrix} \Delta i_d \\ \Delta i_q \end{bmatrix} = - \begin{bmatrix} L_1(s) & 0 \\ 0 & L_2(s) \end{bmatrix} \cdot \begin{bmatrix} s/\omega_{base} & -\omega_0 \\ \omega_0 & s/\omega_{base} \end{bmatrix}^{-1} \cdot \begin{bmatrix} -\psi_{q0} \\ \psi_{d0} \end{bmatrix} \cdot \Delta \omega_r \\ + \begin{bmatrix} L_1(s) & 0 \\ 0 & L_2(s) \end{bmatrix} \cdot \begin{bmatrix} s/\omega_{base} & -\omega_0 \\ \omega_0 & s/\omega_{base} \end{bmatrix}^{-1} \cdot \begin{bmatrix} \Delta u_d \\ \Delta u_q \end{bmatrix}. \quad (10)$$

Equations (7)–(10) reflect the formation mechanism of SG electromagnetic torque, thus giving the formation mechanism diagram shown in Figure 3a. The SG speed disturbance is the input signal, and the electromagnetic torque is composed of two branches, of which the first branch is mainly determined by the SG electrical part and the second branch is codetermined by the SG electrical part and the grid. The expressions of $G_1(s)$, $G_2(s)$, $G_3(s)$, $G_4(s)$, and $G_5(s)$ in Figure 3b are shown in Equation (A1) (Appendix A).

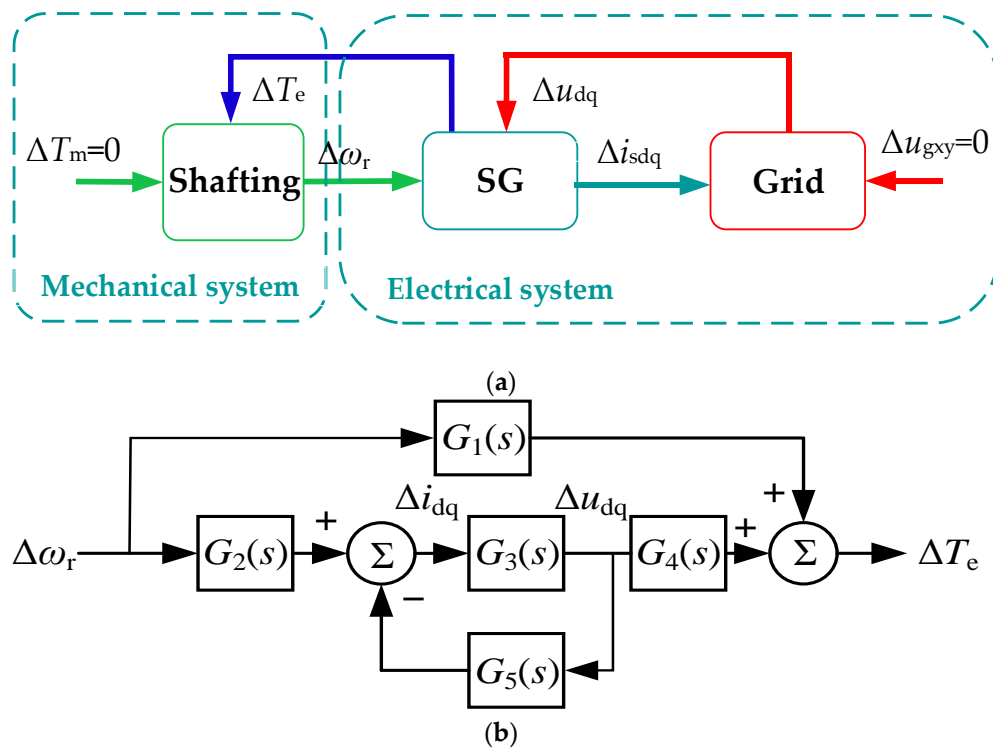


Figure 3. The electromagnetic torque formation mechanism of a synchronous generator (SG): (a) SG electromechanical coupling mechanism; (b) speed disturbance transfer relationship.

It can be seen from Figure 3 that the SG speed disturbance transfer function can be obtained.

$$\Delta T_e = \left\{ G_1(s) + (G_2(s) \cdot G_3(s) \cdot [1 - G_3(s) \cdot G_5(s)]^{-1} \cdot G_4(s)) \right\} \cdot \Delta \omega_r. \quad (11)$$

When the DFIG and HVDC are connected to the system, the mechanism of interaction with the SG is shown in Figure 4. It can be seen that the rotor disturbance $\Delta \omega_r$ of the SG is the input disturbance of the electrical system. The output current disturbance Δi_{sdq} is formed through the electromagnetic coupling relationship of the electrical part. On the one hand, Δi_{sdq} directly forms the electromagnetic torque disturbance ΔT_e and acts on the rotor; on the other hand, the terminal voltage disturbance Δu_{dq} of the SG, wind turbines, and HVDC is formed by the grid coupling. The SG terminal voltage disturbance through its electromagnetic coupling relationship intensifies ΔT_e and Δi_{sdq} ; then, Δi_{sdq} interacts with the terminal voltage disturbances of wind turbines and HVDC to produce current disturbances Δi_{rdq} and Δi_{hdq} . Furthermore, Δi_{rdq} and Δi_{hdq} are superimposed to continue the grid function and form a new terminal voltage disturbance Δu_{dq} , which further aggravates ΔT_e until the system rebalances or loses stability.

It can be seen from Figure 4 that the rotational speed disturbance transfer function among the DFIG, HVDC, and SG is considered as shown in Equation (12).

$$\Delta T_e = \left\{ G_1(s) + (G_2(s) \cdot G_3(s) \cdot [1 - G_3(s) \cdot (G_5(s) + G_{DFIGs}(s) + G_{HVDC}(s))]^{-1} \cdot G_4(s)) \right\} \cdot \Delta \omega_r. \quad (12)$$

of the rotation speed after the disturbance is removed, the electromechanical coupling characteristics among the wind turbines, HVDC, and SGs can be judged, and then the contribution of each equipment to the shaft torsional vibration of the unit can be identified.

Taking the rotor motion equation as an example, the variation rules of rotor angle and its frequency are as follows when there is external disturbance:

$$\Delta \ddot{\delta}_k + 2\sigma_k \Delta \dot{\delta}_k + \omega_{nk}^2 \Delta \delta_k = -\Delta T_{ek}, \quad (13)$$

where the electromagnetic torque $\Delta T_{ek} = -A \cos(\omega_s t)$.

Assuming the angle increment $\Delta \delta_k(t=0) = 0$, the torsional vibration of SG can be expressed as

$$\begin{cases} \Delta \delta_k = \Delta \delta_{k,t}(t) + \Delta \delta_{k,s}(t) \\ \Delta \delta_{k,t}(t) = -B e^{-\sigma_k t} \left(\cos \phi \cos \omega_d t + \frac{\omega_s \sin \phi + \sigma_k \cos \phi}{\omega_d} \sin \omega_d t \right) \\ \Delta \delta_{k,s}(t) = B \cos(\omega_s t - \phi) \end{cases}, \quad (14)$$

$$\begin{cases} B = \frac{A}{\sqrt{(\omega_{nk}^2 - \omega_s^2)^2 + 4\sigma_k^2}} \\ \phi = \arctan \frac{2\sigma_k / \omega_{nk}}{1 - (\omega_s / \omega_{nk})^2} \\ \omega_d = \sqrt{\omega_{nk}^2 - \sigma_k^2} \end{cases}, \quad (15)$$

where $\Delta \delta_{k,t}(t)$ is the transient response that only exists for a period of time, and $\Delta \delta_{k,s}(t)$ is the forced response under the excitation of the injected signal. It can be seen that the SG rotor dynamic process contains attenuation components and forced excitation, and the attenuation coefficient can characterize the modal damping of the system.

When the excitation signal is removed, the rotational speed of the torsional vibration mode decays exponentially. Solving Equation (16) can obtain the expression of shafting torsional vibration, which can be expressed as shown in Equations (17) and (18).

$$\begin{cases} \Delta \ddot{\delta}_k + 2(\sigma_k + \sigma_{ek}) \Delta \dot{\delta}_k + \omega_{nk}^2 \Delta \delta_k = 0 \\ \Delta \delta_k(t_0) = \Delta \delta_{k,0} \end{cases}, \quad (16)$$

$$\Delta \delta_k(t) = C_\theta e^{-\Sigma \sigma_k(t-t_0)} \sin(\omega_d(t-t_0) + \phi), \quad t \geq t_0, \quad (17)$$

$$\Delta \omega_k(t) = C_\omega e^{-\Sigma \sigma_k(t-t_0)} \cos(\omega_d(t-t_0) + \phi), \quad t \geq t_0, \quad (18)$$

where C_θ , C_ω are coefficients, and t_0 is the time to remove the excitation. It can be seen from Equation (18) that, after the excitation is withdrawn, the modal speed changes in the form of attenuated oscillation, and the attenuation rate is the sum of mechanical damping and electrical damping. The total mode can be obtained by identifying the attenuation rate of the torsional vibration mode speed after removing the excitation.

The basic principle of the additional excitation signal injection method is shown in Figure 5 [25], which shows that the modal signal generator superimposes the excitation test signal u_s with controllable angular velocity, amplitude, and duration to the output of automatic voltage regulator (AVR). The u_s can generate the electromagnetic torque disturbance ΔT_e , and it excites a safe and controllable SSO in shafting system. After removing u_s , the change in generator speed depends on the result of the interaction between the mechanical damping and electrical damping of the system, and the damping can be identified using the spectrum analysis method on the basis of discrete Fourier transform. Since the influence of mechanical damping is not considered in this paper, the mechanical damping was set as 0. The main process of the injection method is depicted in Figure 6.

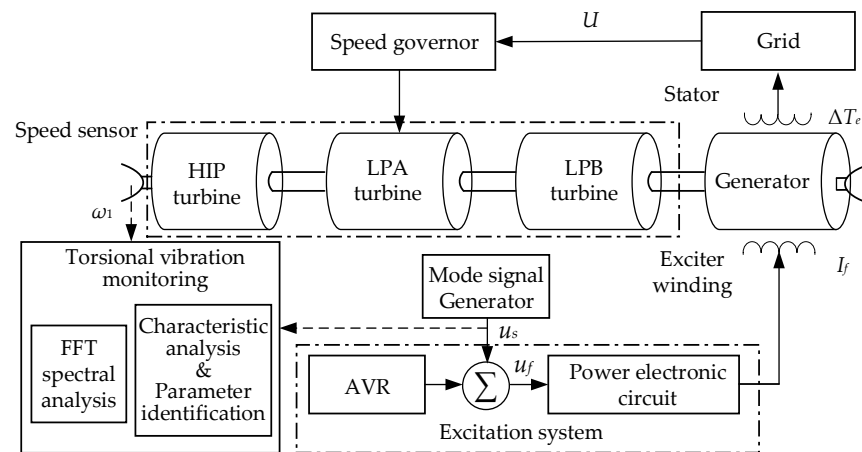


Figure 5. Basic principle of excitation-signal-injection method.

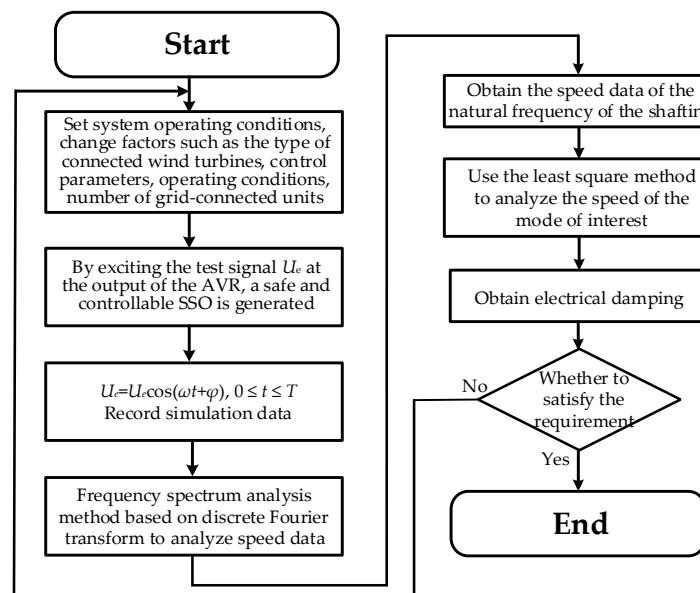


Figure 6. Flowchart of the proposed identification approach.

4.2. Influence of Access to Various Equipment on SG Damping Characteristics

In order to illustrate the feasibility of the above method, the system shown in Figure 1 was taken as an example. The transmission capacity of HVDC was 800 MW, and the output power of the SG was 600 MW. The installed capacity of a single DFIG was 1.5 MW, and the grid-connected number and wind speed of DFIG were 1500 and 4 m/s.

When $t = 0$ s, the excitation signal disturbance was added, and then the signal was removed at 15 s. The rotational speed curve of SG shafting in torsional vibration mode is shown in Figure 7. The logarithm of the ω_r amplitude was taken and curve-fitting was performed. The fitting results are shown in Figure 8, and the attenuation coefficients of TM1–TM4 were -0.1235 , -0.007909 , -0.02113 , and -0.06042 , respectively.

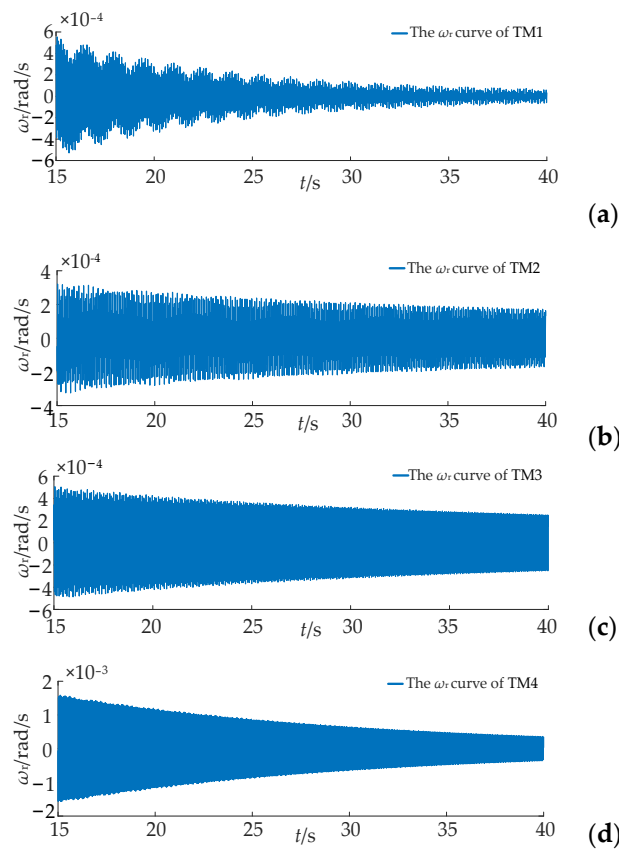


Figure 7. The rotor speed curve of SG torsional mode after repealing the disturbance: (a) TM1; (b) TM2; (c) TM3; (d) TM4.

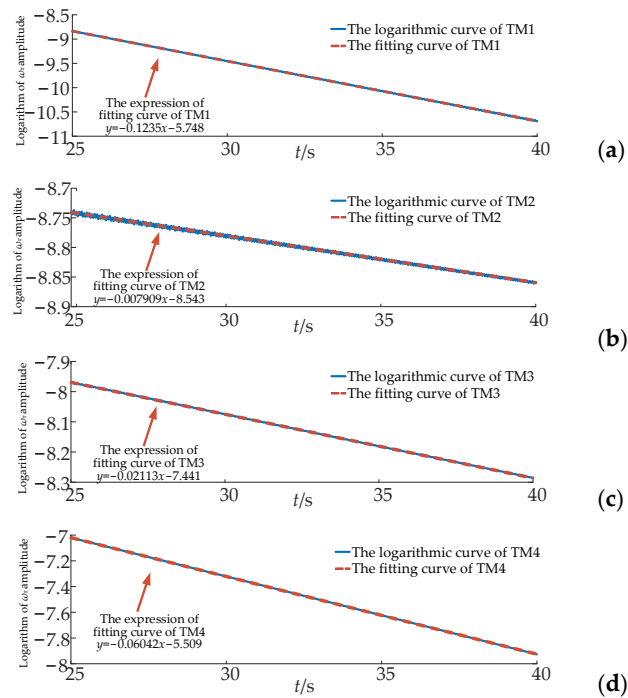


Figure 8. The comparison diagram of the change curves of the amplitude of ω_r after taking the logarithm and fitting curves: (a) TM1; (b) TM2; (c) TM3; (d) TM4.

In order to further analyze the influence of wind speed and control parameters on the torsional vibration of the SG shafting system under the condition of fixed HVDC transmission capacity, the evolution law of the influence of various factors on the torsional vibration was studied by taking a single-DFIG model and a two-machine parallel model as examples.

4.2.1. Influence of Access to Single Equivalent DFIG on SG Shafting

The wind speed was 4 m/s, the transmission capacity of HVDC was 800 MW, the output power of the SG was 600 MW, and the installed capacity of a single DFIG was 1.5 MW. When 1500 units were connected in parallel, the attenuation coefficient of each SG torsional vibration mode was as shown in Figure 9 under the control parameters of different DFIG rotor converter current inner loops.

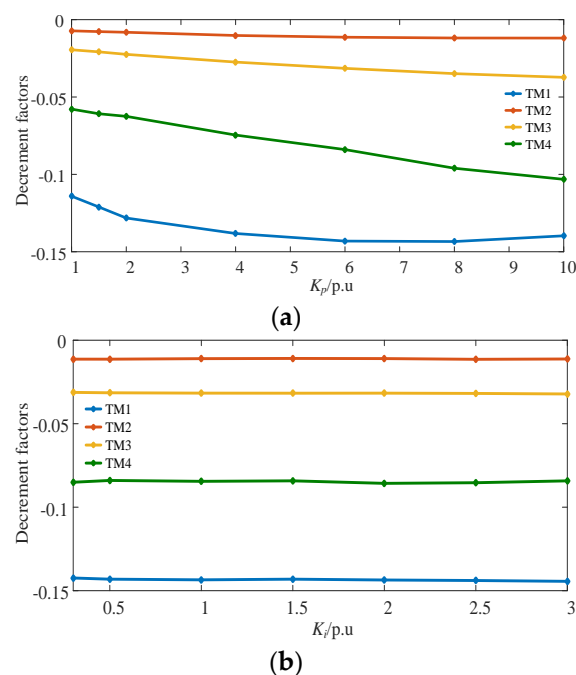


Figure 9. Damping coefficient for each torsional mode of SG under different rotor converter current inner loops: (a) different K_p ; (b) different integral coefficient of the current inner loop (K_i).

It can be seen from Figure 9 that, when the number of grid-connected DFIGs was given, and when K_p changed from 1 p.u. to 10 p.u., the attenuation coefficients of the torsional vibration modes of SG shafting generally showed a trend of decrease, whereby the attenuation coefficient of TM1 decreased 1.2-fold, the attenuation coefficients of TM2 and TM3 decreased 1.7-fold and 1.9-fold, and the attenuation coefficient of TM4 decreased 1.8-fold. The damping characteristics of the modes were enhanced, and, within the same time range, TM1 changed more obviously. As the integral coefficient of the current inner loop increased, the attenuation coefficients of the torsional modes of the SG did not change significantly.

The installed capacity of a single DFIG was 1.5 MW, the output power of the SG was 600 MW, and the output power of HVDC remained at 800 MW. Under different operating conditions of grid-connected DFIGs, the attenuation coefficients of the torsional mode of the SG were as shown in Figure 10.

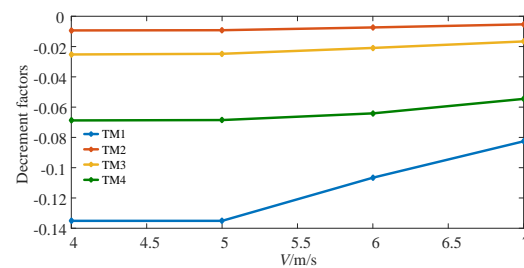


Figure 10. Damping coefficient for each torsional mode of SG under different operating conditions.

It can be seen from Figure 10 that, as the wind speed increased from 4 m/s to 7 m/s, the attenuation coefficients of the torsional modes of SG shafts increases, and the mode damping characteristics weakened. Specifically, the attenuation coefficients of TM1–TM4 increased 1.6-fold, 1.8-fold, 1.5-fold, and 1.3-fold, respectively.

From all the above results, it can be seen that the K_i of DFIGs, as well as the operating conditions of the wind turbines, can affect the damping characteristics of the SG, while the setting of K_i has little effect on the SG damping characteristic.

4.2.2. Influence of Parallel Connection of Two DFIGs on SG Shafting

Considering that the actual wind turbines are often distributed in different regions, the wind speed and the number of grid-connected units in different regions may be quite different. Therefore, this section takes two DFIGs in parallel as an example, considering the geographical distribution of wind turbines; furthermore, it studies the influence of the control parameters and the change in operating conditions on SG shafting in a wind-thermal bundled system transmitted via HVDC.

When the operating condition of DFIGs was 4 m/s, the number of grid-connected units was 1500, and the output power of HVDC and SG was 800 MW and 600 MW, respectively, the K_p of the two DFIGs increased from 1 p.u to 10 p.u. The attenuation coefficient of TM1 of the SG shafting system is shown in Table 1, and the other modes are shown in Tables A4–A6 (Appendix B); in the same way, the current inner loop control integral coefficients of the two DFIGs increased from 0.5 p.u to 3 p.u. The attenuation coefficient of TM1 is shown in Table 2. Tables 1 and 2 show that (1) when the K_p of group1 was constant, with the increase in K_p of the current inner loop of group2, the damping characteristics of the system were enhanced and the oscillation frequency decreased, (2) when the K_i of group1 was constant, with the increase in K_i of group2, the damping characteristics of the SG shafting system changed little, and (3) in the two-DFIG parallel system, the increase in proportional coefficient of the DFIG inner loop was conducive to the stability of TM1, and the change trend was basically the same as the conclusion of the single system.

Table 1. Damping coefficient for TM1 of SG under different K_p .

		Group 1			
		1 p.u	3 p.u	6 p.u	10 p.u
Group 2	1 p.u	−0.1137	−0.125	−0.1291	−0.1262
	3 p.u	−0.125	−0.1339	−0.1371	−0.1373
	6 p.u	−0.1291	−0.1371	−0.1412	−0.1418
	10 p.u	−0.1262	−0.1373	−0.1418	−0.1375

Table 2. Damping coefficient for TM1 of SG under different K_i .

		Group 1			
		0.5 p.u	1.5 p.u	2 p.u	3 p.u
Group 2	0.5 p.u	−0.1412	−0.1427	−0.1425	−0.1427
	1.5 p.u	−0.1427	−0.1438	−0.1427	−0.1432
	2 p.u	−0.1425	−0.1427	−0.1436	−0.143
	3 p.u	−0.1427	−0.1432	−0.143	−0.1428

When K_p was 3 p.u, the capacity of HVDC was 800 MW, and the SG output power was 600 MW, the operating condition of the DFIGs increased from 4 m/s to 7 m/s, and the attenuation coefficient of SG shafting torsional (TM1) was as shown in Table 3. It can be seen from Table 3 that with the increase in wind speed of Group 2, the damping characteristics of the system weakened and the oscillation frequency increased as the wind speed of group1 was constant. Therefore, in the two-machine parallel system, the increase in DFIG operating conditions was harmful to the stability of TM1, and the change trend was consistent with the conclusion of the single system.

Table 3. Damping coefficient for TM1 of SG under different operating conditions.

		Group 1			
		4 m/s	5 m/s	6 m/s	7 m/s
Group 2	4 m/s	−0.1339	−0.1376	−0.1219	−0.1071
	5 m/s	−0.1376	−0.1345	−0.1224	−0.1085
	6 m/s	−0.1219	−0.1224	−0.107	−0.09429
	7 m/s	−0.1071	−0.1085	−0.09429	−0.08924

4.2.3. Influence of SG Parameters on SG Shafting

The influence of SG parameters on the torsional vibration of SG shafting were not considered in the above analysis. This section mainly analyzes the influence of AVR and mechanical damping coefficient of SG on the torsional modes of each shafting. The AC exciter adopts the IEEE AC exciter module AC1A, and the transfer function block diagram is shown in Figure A1 (Appendix C).

When the wind speed of the DFIGs was 4 m/s, the number of grid-connected units was 1500, the HVDC transmission power was 800 MW, and the output power of the SG was 600 MW, under different AVR control parameters (K_A and T_A), the attenuation coefficients of each torsional mode of SG were as shown in Tables 4 and 5. The attenuation coefficients of each torsional mode of SG are shown in Table 6 under different mechanical damping coefficients (D_m).

Table 4. Damping coefficient for TM1–TM4 of SG under different K_A ($T_A = 0.02$).

K_A	TM1	TM2	TM3	TM4
50	−0.1206	−0.008813	−0.0217	−0.02252
150	−0.1207	−0.008823	−0.02172	−0.02255

Table 5. Damping coefficient for TM1–TM4 of SG under different T_A ($K_A = 50$).

T_A	TM1	TM2	TM3	TM4
0.02	−0.1206	−0.008813	−0.0217	−0.02252
0.2	−0.1206	−0.008816	−0.0217	−0.02253

Table 6. Damping coefficient for TM1–TM4 of SG under different T_A ($K_A = 50$).

D_m	TM1	TM2	TM3	TM4
0.05 p.u.	−0.1762	−0.0154	−0.1021	−0.08473
0.1 p.u.	−0.2128	−0.02149	−0.1182	−0.1009
0.2 p.u.	−0.2487	−0.03367	−0.1311	−0.1332

From Tables 4–6, it can be seen that the change in AVR control parameters had little influence on each torsional mode of the SG. The mechanical damping coefficient had a great influence on the torsional mode of the SG, whereby larger coefficients were more conducive to the stability of each torsional mode.

5. Time-Domain Simulation Verification

In order to verify the correctness of the theoretical analysis, a simulation model of DFIGs, SGs, and HVDC connected to a grid system was built in EMTDC/PSCAD. Among them, the SG adopted the IEEE SSR first standard model, and the simulation parameters of SG were as shown in [17]. The HVDC adopted the CIGRE Benchmark Model, whose rated transmission power was 1000 MW. The simulation parameters of HVDC and DFIG are shown in Tables A10 and A11 (Appendix C).

5.1. Influence of Single Machine on Torsional Vibration of SG Shafting

5.1.1. Different Current Inner Loop Control Parameters

The wind speed of the DFIGs was 4 m/s, the number of grid-connected units was 1500, the HVDC transmission power was 800 MW, and the output power of the SG was 600 MW. A three-phase short circuit fault occurred in the system at $t = 6$ s, and the duration was 75 ms. The SG rotor speed response curve under the K_p of DFIGs is shown in Figure 11a. Time–frequency analysis was used to analyze the rotor speed data, and the time–frequency analysis results are shown in Figure 11b,c.

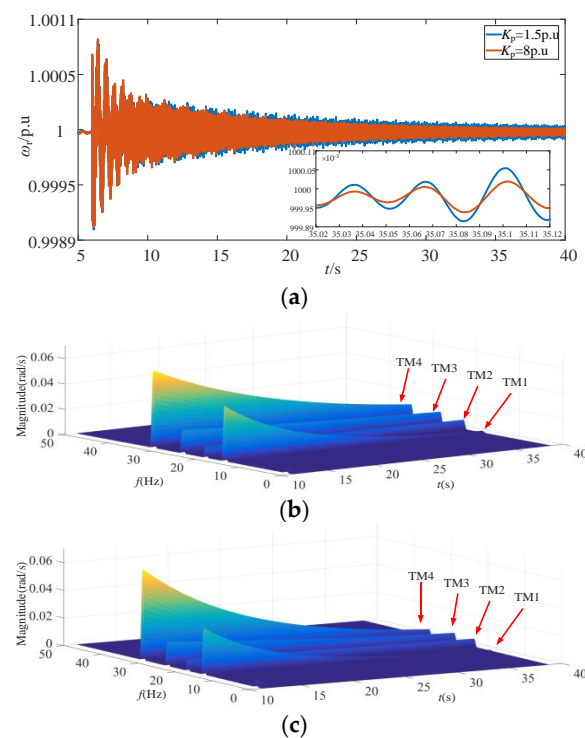


Figure 11. Rotor speed response of SG and the time–frequency analysis result: (a) rotor speed response curve; (b) $K_p = 1.5$ p.u.; (c) $K_p = 8$ p.u.

As can be seen from Figure 11, with the increase in K_p , the attenuation trend of TM1 changed most significantly compared with other modes, and the mode damping was enhanced. The time-domain simulation results were consistent with the analysis results in Section 4.2.1.

5.1.2. Different Operation Conditions

When the control parameters of the DFIGs were constant, the number of grid-connected units was 1500, and the output powers of the HVDC and the SG were fixed, the system had a three-phase short circuit fault at $t = 6$ s with a duration of 75 ms. The results of the rotor speed response curve and time–frequency analysis under different operating conditions of DFIGs are shown in Figure 12.

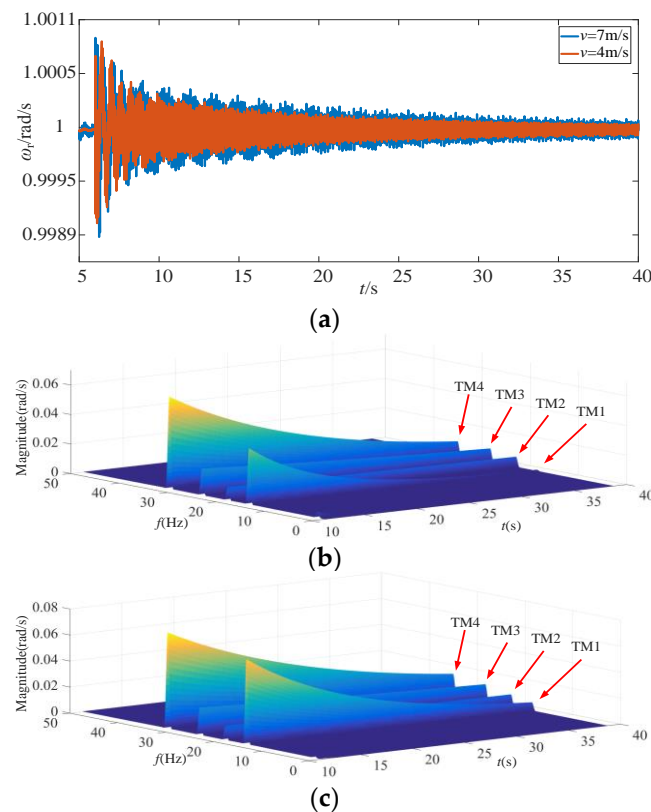


Figure 12. Rotor speed response of SG and the time–frequency analysis result: (a) rotor speed response curve; (b) $v = 4$ m/s; (c) $v = 7$ m/s.

Comparing Figure 12b with Figure 12c, it can be concluded that, when the wind speed of DFIGs increased from 4 m/s to 7 m/s, the change trend of TM1 was more obvious than the other three modes and TM1 damping became weaker, which was not conducive to system stability. The change trend was consistent with the identification results in Figure 10.

5.2. Influence of Two-Machine Parallel System on Torsional Vibration of SG Shafting

The system parameters were the same as in Section 5.1. In this section, the two-machine parallel system was simulated and verified. The torsional vibration of the SG transmitted via an HVDC system was analyzed, accounting for the regional differences in wind turbines, caused by different current inner loop control parameters, operating conditions, and the number of grid-connected units. The results of the SG rotor speed response curve and the time–frequency analysis are shown in Figures 13 and 14.

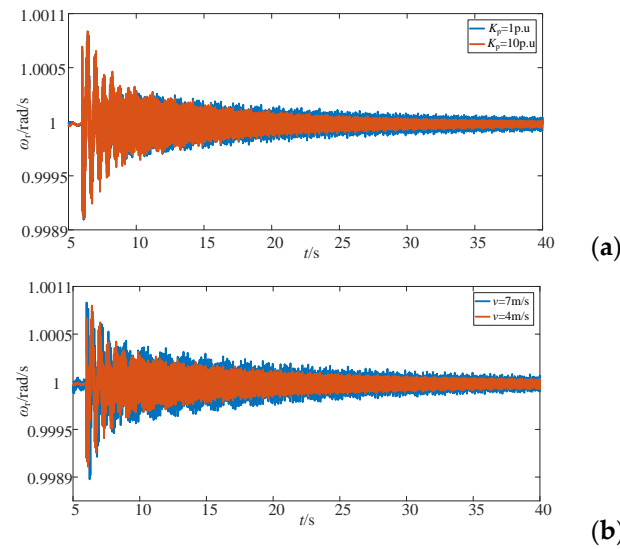


Figure 13. Rotor speed response of SG: (a) $K_p = 1$ p.u.–10 p.u.; (b) $v = 7$ m/s–4 m/s.

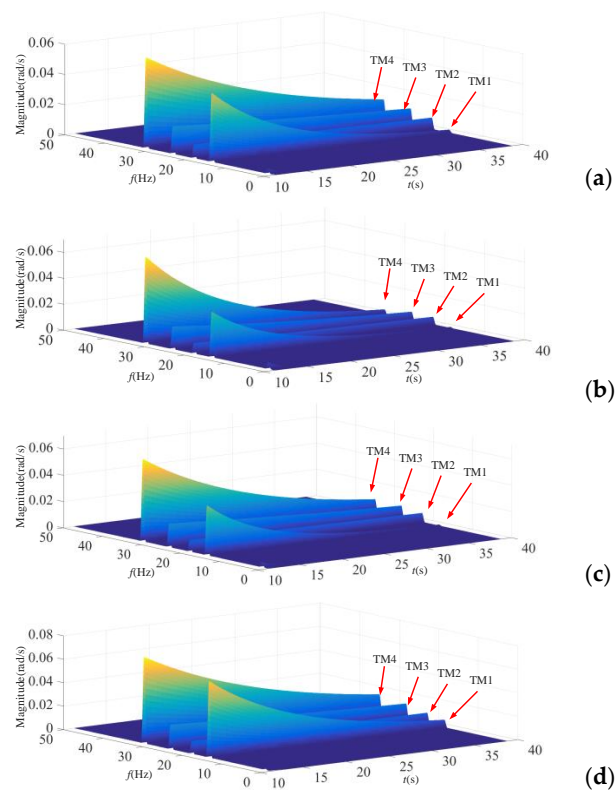


Figure 14. Rotor speed response of SG and the time–frequency analysis result: (a) $K_p = 1$ p.u.; (b) $K_p = 10$ p.u.; (c) $v = 4$ m/s; (d) $v = 7$ m/s.

From the time-domain analysis, it can be seen that, when the K_p of the RSC in the DFIG increased and the operating conditions decreased, it was conducive to the stability of the system.

6. Conclusions

This paper proposed a torsional vibration analysis method for a system containing HVDC, DFIGs, and SGs, using the additional excitation signal injection method. It revealed the torsional modes of the SG shafting caused by DFIGs connected to the grid. The main conclusions are as follows:

(1) In a typical wind–thermal bundled system transmitted via HVDC, the electromagnetic transient process among wind turbines, SGs, and HVDC influences the electromechanical transient process of the system. There are some factors, such as the types of grid-connected wind turbines, main control parameters, operating conditions, and; the transmission power and control parameters of HVDC that affect the torsional modes of the SG to some extent.

(2) For the DFIG and SG system transmitted via HVDC, under the given HVDC transmission capacity, as the current inner loop control parameters of the RSC of the DFIG decreased ($K_p = 10$ p.u–1 p.u), the damping characteristics of each torsional mode of the SG decreased; as the operating conditions of the DFIG decreased ($v = 7\text{--}4$ m/s), the damping characteristics of each torsional mode gradually increased. With the increase in mechanical damping coefficient ($D_m = 0.05$ p.u–2 p.u), the damping of each torsional mode increased, which was beneficial to the stability of the system.

Author Contributions: Conceptualization, Q.J. and G.Y.; methodology, Q.J.; software, J.W.; validation, J.W. and K.L.; formal analysis, D.W.; investigation, J.W. and K.L.; resources, Q.J.; data curation, J.W.; writing—original draft preparation, J.W.; writing—review and editing, J.W.; visualization, Q.J.; supervision, G.Y.; project administration, G.Y.; funding acquisition, G.Y. All authors have read and agreed to the published version of the manuscript.

Funding: This research was funded by the Joint Fund of the National Natural Science Foundation of China, grant number U1866601.

Conflicts of Interest: The authors declare no conflict of interest.

Appendix A

Table A1. The definitions of variables for the DFIG.

Variable	Notation
Reactive power of stator	Q_s
Active power of stator	P_s
Reactive power of grid	Q_g
Voltage of rotor	u_r
Current of rotor	i_r
Voltage of grid	u_g
Current of grid	i_g
Voltage of stator	u_s
DC capacitor voltage	u_{dc}
Direct current capacitor	C_{dc}
Connection reactance	L_c
Output phase of phase-locked loop	θ_{PLL}
Wind speed	v
Rotor speed	ω_r
The flux linkage of stator	ψ_s
The flux linkage of rotor	ψ_r
Output voltage of GSC	u_{cg}
Output current of GSC	i_{cg}
Inductance of GSC	L_1
Inductance of rotor	L'
Rated angular speed of the stator	ω_0
Slip	s
Mutual reactance	x_m
Reactance of the stator	x_s
State variables in the control system	$x_1 \sim x_8$

Table A2. The definitions of variables for the SG.

Variable	Notation
Stator voltage	U_{dq}
Stator current	i_{dq}
Stator linkage	ψ_{dq}
Current of excitation winding	i_f
Current of damping winding in the d-axis	i_D
Current of damping winding in the g-axis	i_g
Current of damping winding in the Q-axis	i_Q
Voltage of exciter	E_{fd}
Location of speed relay	α
Opening angle of valve	μ
Motive power of steam turbine	$T_1 \sim T_3$
Rotational speed of 6-mass	$\omega_1 \sim \omega_6$
Rotor phase of 6-mass	$\delta_1 \sim \delta_6$

$$\left\{ \begin{array}{l}
 G_1(s) = - \left\{ \begin{bmatrix} i_{q0} & -i_{d0} \end{bmatrix} + \begin{bmatrix} -\psi_{q0} & \psi_{d0} \end{bmatrix} \cdot \begin{bmatrix} L_1(s) & 0 \\ 0 & L_2(s) \end{bmatrix} \right\} \cdot \begin{bmatrix} s/\omega_{base} & -\omega_0 \\ \omega_0 & s/\omega_{base} \end{bmatrix}^{-1} \cdot \begin{bmatrix} -\psi_{q0} \\ \psi_{d0} \end{bmatrix} \\
 G_2(s) = - \begin{bmatrix} L_1(s) & 0 \\ 0 & L_2(s) \end{bmatrix} \cdot \begin{bmatrix} s/\omega_{base} & -\omega_0 \\ \omega_0 & s/\omega_{base} \end{bmatrix}^{-1} \cdot \begin{bmatrix} -\psi_{q0} \\ \psi_{d0} \end{bmatrix} \\
 G_3(s) = \begin{bmatrix} Z_{11} & Z_{12} \\ Z_{21} & Z_{22} \end{bmatrix} \\
 G_4(s) = \left\{ \begin{bmatrix} i_{q0} & -i_{d0} \end{bmatrix} + \begin{bmatrix} -\psi_{q0} & \psi_{d0} \end{bmatrix} \cdot \begin{bmatrix} L_1(s) & 0 \\ 0 & L_2(s) \end{bmatrix} \right\} \cdot \begin{bmatrix} s/\omega_{base} & -\omega_0 \\ \omega_0 & s/\omega_{base} \end{bmatrix}^{-1} \\
 G_5(s) = \begin{bmatrix} L_1(s) & 0 \\ 0 & L_2(s) \end{bmatrix} \cdot \begin{bmatrix} s/\omega_{base} & -\omega_0 \\ \omega_0 & s/\omega_{base} \end{bmatrix}^{-1}
 \end{array} \right. \tag{A1}$$

Table A3. The definitions of variables for HVDC.

Variable	Notation
AC system voltage	V_r
AC system current	I_r
DC line current	I_{dc}
DC line capacitance voltage	V_{dc}
AC bus voltage	V_{PCC}
Filter capacitance voltage	V_{cr}
Filter capacitance current	I_{Lr}
State variables in the phase-locked loop controller	$x_9 \sim x_{10}$
State variables in the current loop controller	$x_{11} \sim x_{12}$

Appendix B

Table A4. Damping coefficient for TM2 of SG under different K_p .

Group 2 \ Group 1	0.01	0.03	0.06	0.10
	0.01	-0.007161	-0.008144	-0.008696
0.03	-0.008144	-0.009209	-0.01047	-0.00998
0.06	-0.008696	-0.01047	-0.01127	-0.01153
0.10	-0.008758	-0.00998	-0.01153	-0.01187

Table A5. Damping coefficient for TM3 of SG under different K_p .

		Group 1			
		0.01	0.03	0.06	0.10
Group 2	0.01	−0.01933	−0.02213	−0.02481	−0.0267
	0.03	−0.02213	−0.02492	−0.02751	−0.03029
	0.06	−0.02481	−0.02751	−0.03117	−0.03423
	0.10	−0.0267	−0.03029	−0.03423	−0.03682

Table A6. Damping coefficient for TM4 of SG under different K_p .

		Group 1			
		0.01	0.03	0.06	0.10
Group 2	0.01	−0.05832	−0.06379	−0.06968	−0.07934
	0.03	−0.06379	−0.06961	−0.07486	−0.0854
	0.06	−0.06968	−0.07486	−0.08635	−0.09565
	0.10	−0.07934	−0.0854	−0.09565	−0.1061

Table A7. Damping coefficient for TM2 of SG under different operating conditions.

		Group 1			
		4 m/s	5 m/s	6 m/s	7 m/s
Group 2	4 m/s	−0.009209	−0.009532	−0.008106	−0.007434
	5 m/s	−0.009532	−0.009037	−0.007951	−0.007308
	6 m/s	−0.008106	−0.007951	−0.007347	−0.006515
	7 m/s	−0.007434	−0.007308	−0.006515	−0.006187

Table A8. Damping coefficient for TM3 of SG under different operating conditions.

		Group 1			
		4 m/s	5 m/s	6 m/s	7 m/s
Group 2	4 m/s	−0.02492	−0.02601	−0.02296	−0.02096
	5 m/s	−0.02601	−0.02437	−0.02296	−0.02103
	6 m/s	−0.02296	−0.02296	−0.02112	−0.01892
	7 m/s	−0.02096	−0.02103	−0.01892	−0.0183

Table A9. Damping coefficient for TM4 of SG under different operating conditions.

		Group 1			
		4 m/s	5 m/s	6 m/s	7 m/s
Group 2	4 m/s	−0.06961	−0.06708	−0.0659	−0.06452
	5 m/s	−0.06708	−0.06817	−0.0668	−0.06279
	6 m/s	−0.0659	−0.0668	−0.06526	−0.06163
	7 m/s	−0.06452	−0.06279	−0.06163	−0.05618

Appendix C

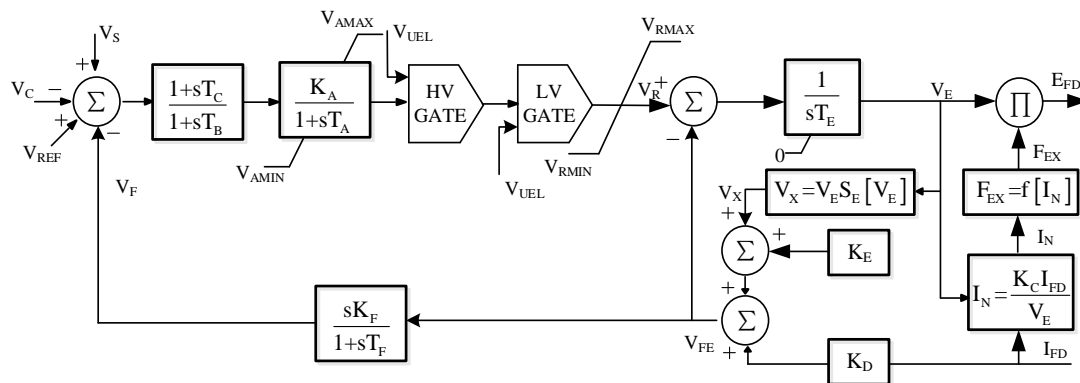


Figure A1. The transfer function of AC1A.

Table A10. Main parameters of the DFIG.

Parameter	Unit/p.u.
Nominal capacity of DFIG P_{DFIG}	1.5
Voltage of grid u_g	0.69
Resistance of the stator r_s	0.0164
Reactance of the stator x_s	0.255
Resistance of the rotor r_r	0.0183
Reactance of the rotor x_r	0.222
Mutual reactance x_m	13.68
DC capacitor voltage u_{dc}	1.5
Direct current capacity C_{dc}	0.09
Inductance of rotor L'	0.005
Inductance of GSC L_1	0.005

Table A11. Parameters of the HVDC controller.

Parameter	Unit/p.u.
Proportional coefficient of constant current controller K_{Pr}	1.0989
Integral coefficient of constant current controller K_{ir}	1/0.01092
Proportional coefficient of turn-off angle controller K_{Pi}	0.7506
Integral coefficient of fixed turnoff angle controller K_{ii}	1/0.0544
Proportional coefficient of measuring link K_{mr}	0.5
Integral coefficient of measuring link T_{mr}	0.0012
proportional coefficient of PLL K_{pPLL}	10
Integral coefficient of PLL K_{iPLL}	50
Proportional coefficient of constant current controller K_{Pr}	1.0989
Integral coefficient of constant current controller K_{ir}	1/0.01092
Proportional coefficient of turn-off angle controller K_{Pi}	0.7506

References

- Joselin, H.G.M.; Iniyar, S.; Sreevalsan, E.; Rajapandian, S. A review of wind energy technologies. *Renew. Sustain. Energy Rev.* **2007**, *11*, 1117–1145. [CrossRef]
- Ackermann, T. *Wind Power in Power System*; Wiley: Chichester, UK, 2005; pp. 7–23.
- China National Energy Administration. Operation of Wind Farm in First Half of 2020. Available online: http://www.nea.gov.cn/2020-07/31/c_139254298.htm (accessed on 31 July 2020).
- Energy Research Institute National Development and Reform Commission. *China 2050 High Renewable Energy Penetration Scenario and Roadmap Study*; Energy Research Institute National Development and Reform Commission: Beijing, China, 2015.
- Shair, J.; Xie, X.; Wang, L.; Liu, W.; He, J.; Liu, H. Overview of emerging subsynchronous oscillations in practical wind power systems. *Renew. Sustain. Energy Rev.* **2019**, *99*, 159–168. [CrossRef]

6. Xie, X.R.; Liu, H.K.; He, J.B.; Liu, H.; Liu, W. On new oscillation issues of power systems. *Proc. CSEE* **2018**, *38*, 2821–2828.
7. Xie, X.R.; Wang, L.P.; He, J.B.; Liu, H.; Wang, C.; Zhan, Y. Analysis of subsynchronous resonance/oscillation types in power systems. *Power Syst. Technol.* **2017**, *41*, 1043–1049.
8. Li, M.J.; Yu, Z.; Xu, T.; He, J.B.; Wang, C.; Xie, X.; Liu, C. Study of complex oscillation caused by renewable energy integration and its solution. *Power Syst. Technol.* **2017**, *41*, 1035–1042.
9. Bahrman, M.; Larsen, E.V.; Piwko, R.J.; Patel, H.S. Experience with HVDC-turbine-generator torsional interaction at square butte. *IEEE Trans. Power Appar. Syst.* **1980**, *99*, 966–975. [[CrossRef](#)]
10. Piwko, R.J.; Larsen, E.V. HVDC System Control for Damping of Subsynchronous Oscillations. *IEEE Power Eng. Rev.* **1982**, *2*, 58. [[CrossRef](#)]
11. Zhou, C.C.; Xu, Z. Damping analysis of subsynchronous oscillation caused by HVDC. *Proc. CSEE* **2003**. [[CrossRef](#)]
12. Yu, H.Y.; Zhao, G.L.; Hu, Y.T.; Gao, B.F.; Zhang, X.W. Damping characteristics of sub-synchronous torsional interaction of DFIG-based wind farm connected to HVDC system. *J. Eng.* **2017**, *13*, 1934–1939. [[CrossRef](#)]
13. Gao, B.F.; Liu, Y.; Song, R.H.; Zhang, R.X.; Shao, B.B.; Li, R.; Zhao, S.Q. Study on subsynchronous oscillation characteristics of DFIG-based wind farm integrated with LCC-HVDC system. *Proc. CSEE* **2020**, *40*, 3477–3489.
14. Yang, L.; Xiao, X.N.; Pang, C.Z. Oscillation analysis of a DFIG-based wind farm interfaced with LCC-HVDC. *Sci. China Technol. Sci.* **2014**, *57*, 2453–2465. [[CrossRef](#)]
15. Gao, B.F.; Liu, Y.; Li, Y.H.; Zhao, F.; Shao, B.B.; Zhao, S.Q. Analysis on Disturbance Transfer Path and Damping Characteristics of Sub-Synchronous Interaction between D-PMSG-Based Wind Farm and LCC-HVDC. *Proc. CSEE*. Available online: <http://kns.cnki.net/kcms/detail/11.2107.TM.20200603.1139.004.html> (accessed on 4 June 2020).
16. Zhao, S.Q.; Zang, X.W.; Gao, B.F.; Ren, L.; Yang, L. Analysis and countermeasure of sub-synchronous oscillation in wind-thermal bundling system sent out via HVDC transmission. *Adv. Technol. Electr. Eng. Energy* **2018**, *36*, 41–50.
17. Gao, B.F.; Hu, Y.T.; Song, R.H.; Li, R.; Zhang, X.W.; Yang, L.; Zhao, S.Q. Impact of DFIG-based wind farm integration on sub-synchronous torsional interaction between HVDC and thermal generators. *IET Gener. Transm. Distrib.* **2018**, *12*, 3913–3923. [[CrossRef](#)]
18. Bi, Y.; Liu, T.Q.; Zhao, L.; Li, X.Y.; Gu, Y.J. DC additional damping control of subsynchronous oscillation based on improved active disturbance rejection control for wind-thermal-bundled power system. *Electric Power Autom. Equip.* **2018**, *38*, 174–180.
19. Walker, D.N.; Bowler, C.E.J.; Jackson, R.L.; Hedges, D.A. Results of subsynchronous resonance test at Mohave. *IEEE Trans. Power Appar. Syst.* **1975**, *94*, 1878–1889. [[CrossRef](#)]
20. IEEE Subsynchronous Resonance Task Force. First benchmark model for computer simulation of subsynchronous resonance. *IEEE Trans. Power Appar. Syst.* **1977**, *96*, 1565–1572. [[CrossRef](#)]
21. Szechtmann, M.; Wess, T.; Thio, C.V. A benchmark model for HVDC system studies. In Proceedings of the Fifth International Conference on AC and Dc Power Transmission, London, UK, 17–20 September 1991.
22. Fan, L.; Kavasseri, R.; Miao, Z.L.; Zhu, C. Modeling of DFIG-based wind farms for SSR analysis. *IEEE Trans. Power Deliv.* **2010**, *25*, 2073–2082. [[CrossRef](#)]
23. Fan, L.; Zhu, C.; Miao, Z.X.; Hu, M.Q. Modal analysis of a dfig-based wind farm interfaced with a series compensated network. *IEEE Trans. Energy Convers.* **2011**, *26*, 1010–1020. [[CrossRef](#)]
24. Dong, X.L.; Xie, X.R.; Li, J.; Han, Y. Comparative study of the impact on subsynchronous resonance characteristics from the different location of wind generators in a large wind farm. *Proc. CSEE* **2015**, *35*, 5173–5180.
25. Xie, X.R.; Dong, Y.P.; Liu, H.; Kang, J. Identifying torsional modal parameters of large turbine generators based on the supplementary-excitation-signal-injection test. *Electr. Power Energy Syst.* **2014**, *56*, 1–8. [[CrossRef](#)]